State-of-the-Art X-Ray Spectroscopy in Catalysis

State of the art x-ray spectroscopy in catalysis

Jeroen A. van Bokhoven,[1,2,*] and Carlo Lamberti[3,4,*]

[1] Institute for Chemical and Bioengineering, ETH Zürich, CH-8093 Zurich, Switzerland
[2] Swiss Light Source, Paul Scherrer Institute, CH-5232 Villigen PSI, Switzerland. E-mail: j.a.vanbokhoven@chem.ethz.ch / jeroen.vanbokhoven@psi.ch
[3] IRC "Smart Materials", Southern Federal University, Zorge Street 5, 344090 Rostov-on-Don, Russia.
[4] Department of Chemistry, CrisDi Centre for crystallography, NIS interdepartmental center and INSTM reference center, University of Torino, Via Giuria 7, I-10125 Torino, Italy. E-mail: carlo.lamberti@unito.it

After having introduced the basic theoretical background of XAS (both XANES and EXAFS) and XES (both resonant and non-resonant) spectroscopies, we selected four examples where XAS and/or XES were relevant in understanding the local structure and the electronic configuration of active centers on heterogeneous catalysts. The relevance of in situ and operando condition and the need to perform time-resolved experiment experiments has been highlighted.

1. Introduction

Characterization of catalysts by x-ray spectroscopy is very appealing because x-rays have a large penetration depth, which may traverse through a catalytic reactor, thus enabling in situ and operando measurements by placing a reactor holding the catalyst in the x-ray beam.[1-3]. X-ray spectroscopy can be measured in absorption and emission modes and are respectively called x-ray absorption and emission spectroscopy, XAS and XES (vide infra). A unique feature of XAS and XES is that they yield geometric and electronic structure of elements. The local, short-range geometry, such as coordination number, distance to neighbors, and their disorder, and the electronic density, which relates to filled and un-filled densities of state are obtained. The in situ capability, the element-specific nature and the ability to measure crystals, amorphous solids, liquids, and gases are attractive features for catalysis research. Although the emphasis of XAS and XES in catalysis has been on heterogeneous catalysis,[3-8] homogeneous catalytic processes[9] and even solid-liquid-gas systems[10,11] have been accessed.

Catalysts are generally either pressed into self-sustaining pellets or they are pelletized and grinded into particles placed within a tubular reactor. The surrounding gas composition is precisely controlled and catalytic conversion measured at the end of the set-up, by gas chromatography or, mostly, by mass spectrometry.[12,13] Such set-up makes combination with complementary characterization tools possible. Vibrational spectroscopy[14,15] and diffraction are the most-important tools yielding data on the adsorbed intermediates respectively the crystalline parts of the sample.[16].

Heterogeneous reactions occur between chemisorbed species at the surface of a solid, which is the so-called Langmuir Hinshelwood mechanism. Alternatively, a second reactant may react with a surface-attached species in the Eley-Rideal mechanism. In any case, the catalyst forms a chemical bond with one or more of the reacting molecules. In first approximation, it is obvious that in case of extremely weak adsorption, there is very little adsorption and the surface reaction cannot take place; likewise, if adsorption is too strong, the formed catalyst-adsorbate complex is too stable to react and or for any product to desorb. As too weak and too strong adsorption does not lead to efficient catalysts, there is an optimum in bond strength between the active site in a catalyst and adsorbate. Molecular oxygen is an often-used reactant in

oxidation reactions. It's bond strength is about 500 kJ/mol and dissociative adsorption occurs on the catalyst surface. For dissociative adsorption to occur, the bond strength between the oxygen atoms and the catalyst surface must exceed 250 kJ/mol. This strong bonding with oxygen atoms is paralleled by changes in electronic and geometric structure at the catalyst surface. Variation in oxidation state of atoms involved in the catalytic conversion are therefore often observed. To understand the functioning of a catalyst and the reaction mechanism, capturing the structural changes and measuring under in situ reactions are absolutely essential. The catalyst structure before and after will not be representative of that during reaction.
This chapter will briefly introduce the basics of XAS and XES and provide illustrative state-of-the-art examples of how these methods contribute to understanding the catalytic process. Current trends in XA and XE spectroscopy will be identified.

2. X-ray absorption, XA and emission, XE spectroscopy

Figure 1 shows the basic steps of XA and XE processes. Upon irradiation of matter by x-rays, excitation occurs if the photon has sufficient energy to excite the electron into an energy level above the Fermi level (E_F): absorption of the photon occurs, which is at the origin of its name. XA spectroscopy measures the variations of the X-ray absorption coefficient μ as a function of the incident X-ray energy E. According to the Fermi Golden Rule,[17,18] the XAS signal is proportional to the electron transition probability from the core-state |i> of energy E_i to the unoccupied state |f> of energy E_f, as expressed by Eq.(1), where the product **e·r** indicates the electronic transition dipole operator,[19] where $\rho_i(occ)$ and $\rho_f(unocc)$ are the densities of initial occupied and final unoccupied states, respectively, and where $\delta(E_f\text{-}E_i\text{-}E)$ is a Dirac delta function for energy conservation.[20,21]

$$\mu(E) = |< f|\mathbf{e}\cdot\mathbf{r}|i >|^2 \delta(E_f - E_i - E)\rho_i(occ)\rho_f(unocc) \qquad (1)$$

For standard XAS experiment the starting state |i> is fully occupied, consequently, from Eq.(1), it is evident that the likeliness that absorption occurs depends on the empty density of states $\rho_f(unocc)$, which is reflected in the energy dependence of the absorption spectrum.

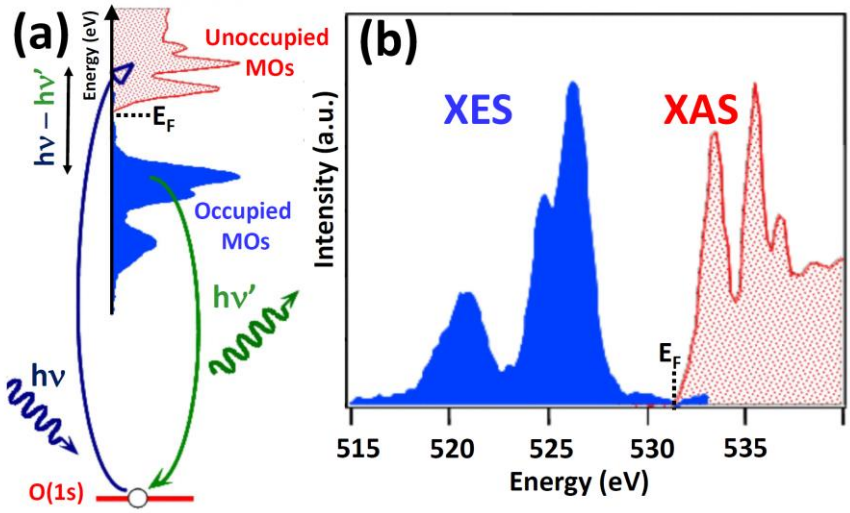

Figure 1. Part (a): scheme representing X-ray absorption, XA, and x-ray emission, XE, processes. In XA, the absorption of a photon with energy hν excites an electron to an unoccupied state above the Fermi level. In XE, a photon with energy hν' is emitted when an electron from a higher shell annihilates the core hole formed in the XA process. Part (b): by scanning the incoming photon energy hν and integrating over the emitted hν' photons (or fixing hν' in case of HRFD-XAS) XAS spectra are obtained (red curve), probing the empty density of states. Fixing the excitation energy hν, and scanning the emission photon energy hν' XES spectra (blue curve) are obtained, they probe the filled density of states. Also shown are the energy transfer (hν – hν') and the Fermi level (E_F, also known as electrochemical potential). Adapted with permission from Ref. [22], copyright SPIE (2007).

Upon excitation of the electron, a core-hole is created. Annihilation of this excited state occurs by filling of the core-hole by electrons of lower binding energy (higher levels); emission of a photon or an electron, the Auger electron, happens, which releases the excess energy. Figure 1 illustrates the emission process for radiative emission. Detection of the energy-dependence of the emitted photons is reminiscent of the energy-dependence of the occupied electronic states. It is finally worth defining the difference between resonant and non-resonant XE. After excitation with x-ray incident energy hν well above an absorption edge of the element of interest, the excited system can relax filling the photo-induced core-hole by radiative decay from a continuum state, resulting in a *non-resonant* x-ray emission. The XES technique relies in the detection of these emitted photons as a function of their energy hν' with an energy resolution at least of the same order of the core hole lifetime broadening. Alternatively, if the system is *resonantly* excited to a localized state (tuning the incident X-ray energy hν to an absorption feature in proximity of the Fermi level E_F), and the subsequent radiative decay is monitored with lifetime energy resolution, the technique is referred to as resonant-XES (r-XES) or resonant inelastic X-ray scattering (RIXS). Both non-resonant XES and r-XES can be described in a common theoretical framework,[4,23-26] modelling the underlying physics as a two-level photon scattering process *via* the Kramers-Heisenberg equation,[27] eq. (2):

$$F(\mathrm{h\nu}, \mathrm{h\nu}') = \sum_f \left| \sum_n \frac{\langle f|T_2|n\rangle\langle n|T_1|i\rangle}{E_i - E_n + \mathrm{h\nu} - i\frac{\Gamma_{INT}}{2}} \right|^2 \cdot \frac{\frac{\Gamma_{FIN}}{2\pi}}{(E_i - E_n + \mathrm{h\nu} - \hbar\omega)^2 + \frac{\Gamma^2{}_{FIN}}{4}} \qquad (2)$$

Eq. (2) expresses the scattered x-ray intensity *F*(hν, hν') as a function of the incident (hν) and emitted (hν') X-ray energy, and of the energies of the electronic configurations; |i>, |n> and |f> indicate the electron wavefunctions for the starting (ground) state, the intermediate and the final state, respectively. Corresponding energies are indicated as E_i, E_n and E_f. Γ_{INT} and Γ_{FIN} express the intermediate and final state lifetime broadenings (in term of FWHM); the operators T_1 and T_2 describe the absorption and the emission of an x-ray photon, respectively. The energy difference hν – hν' represents the energy transfer occurring during the inelastic scattering process, usually used as second axis in the RIXS maps, vide infra Figure 6.

3. Extended x-ray absorption fine structure, EXAFS

In the scheme reported in Figure 1, when the energy of the x-ray photon exceeds the ionization limit (hν – E_B), the excited electron (generally named "photoelectron") has a kinetic energy E_K given by E_K = hν – E_B, where E_B indicates the electron binding energy, that is typical of the absorption edge (K, L_1, L_2 or L_3) of the selected atomic species,[3] around 543 eV for O K-edge.[28] Once ejected, the photoelectron propagates thorough the sample as a spherical wave diffusing from the absorber atom, with a wavevector of modulus k defined by Eq. (3):

$$k = \frac{2\pi}{h}\sqrt{mE_K} \qquad (3)$$

The EXAFS region of the spectrum is characterized by the modulation of the absorption coefficient μ(E) in the high energy range above the edge.[20,29-33] Such feature is caused by the interference between the x-ray waves diffused by the absorber atom and back-scattered by its neighbors. Hence, EXAFS oscillations can be related via Fourier transform to a specific spatial arrangement of the atoms in the local environment of the absorber, bridging the energy space to the real distances *r*-space.[34-36]

The higher photoelectron kinetic energy in the EXAFS region implies that the phenomenon is no more dominated by the full multiple scattering (MS) regime, that instead dominate in the XANES region; consequently data analysis can be performed using the simpler Fourier transform operation. The EXAFS signal χ(E) is generally expressed as the oscillatory part of the

μ(E) function, normalized to the edge-jump, i.e. χ(E) = [μ(E) – μ0(E)]/Δμ0(E), where μ0(E) is the atomic-like background absorption and Δμ0(E) the normalization factor. Above the absorption edge, the energy E can be substituted with the photoelectron wave-vector k using Eq. (3), therefore obtaining the EXAFS function χ(k). The relation between the modulation of the χ(k) signal and the structural parameters is provided by the EXAFS formula that, in the single scattering (SS) approximation, is reported in Eq. (4):

$$\chi(k) = S_0^2 \sum_i N_i F_i(k) e^{-2\sigma_i^2 k^2} e^{-\frac{2r_i}{\lambda(k)}} \frac{\sin\left[2kr_i + 2\delta_l(k) + \theta_i(k)\right]}{kr_i^2} \qquad (4)$$

Where, S_0^2 is the overall amplitude reduction factor; the index i runs over all the different shells of neighboring atoms around the absorber, $F_i(k)$ is the back-scattering amplitude as a function of k for each shell, in N_i is the coordination number (number of equivalent scatterers), σ_i is the Debye-Waller factor accounting for thermal and static disorder, λ(k) is the electron mean free path. The parameter r_i indicates the interatomic distance of the i-th shell from the central absorber. The phase shift of the photoelectron is distinguished in two contributions, related to the absorber ($2\delta_l$) and to the scatterer (θ_i). As the electron scattering is mainly performed by the electron clouds of the neighbor atoms, it is evident that $F_i(k)$ will be larger for larger Z neighbors. Consequently EXAFS will be less efficient in the detection of low Z neighbors and the discrimination among neighbors having similar Z will be critical. When the difference in Z is sufficiently large, then both back-scattering amplitude $F_i(k)$ and phase shift functions are markedly different to allow an easy discrimination between the different neighbors. In the other cases, XES is the more suitable technique.

The actual χ(k) function is the sum over all SS paths, as reported in Eq. (4), plus all multiple scattering (MS) paths, that are paths involving scattering from more than one neighboring atom. As the MS path length ($2r_i$) is larger than the SS ones, usually the intensity of the MS paths is lower than the SS ones, because dumped by the $\exp[-2r_i/\lambda(k)]$, and most of them can be neglected in the data analysis. Exception is made when an almost collinear arrangement of atoms occurs, like for most of the metal-carbonyls, in such cases the intensity of the MS path is enhanced and they must be included in the analysis.[37-40] In Figure 8, in the last example treated in this chapter, we report a detailed EXAFS analysis detailing the different SS and MS contribution to the overall EXAFS signal, where the role of the different terms of Eq. (4) are clearly visible.

4. Selected examples

In the following few relevant examples will be discussed in detail, showing the unique role of XAS and XES in characterizing catalysts under in situ and reaction conditions. In section 4.1, we will show how XANES succeeded in probing the formation of the hydride phase in palladium nanoparticles, discriminating between surface and bulk hydride phases and highlighting the role of the particle size. The direct detection of valence structure in platinum nanoparticles by XES and its modification upon carbon monoxide adsorption is reviewed in section 4.2. In section 4.3 we show how time resolved, resonant-XES collected under operando conditions, was able to discriminate active species from spectators in a ceria-based oxidation catalyst. Finally, the detailed in situ EXAFS and XANES study of the red-ox chemistry of UiO-67-Cu MOF (metal-organic frameworks, representative of a new class of shape selective catalysts) is reviewed in section 4.4.

4.1. Hydrogen in and on palladium: X-ray absorption near-edge spectroscopy, XANES

As discussed in section 2, XANES probes empty density of states, see Figure 1 and Eq.(1). The most-used electron excitations are those from the 1s, 2s and 2p orbitals. They yield the empty p-DOS for 1s and 2s excitation and are the K respectively L_1 edges. Excitation of a 2p electron yields both the empty s- and d-DOS and are the L_2 and L_3 edges, depending on the spin states. Bonding of adsorbates to surfaces yields bonding, anti-bonding and non-bonding states (Figure 2), the latter two can be probed in XA, while the bonding states are accessible by XE (Figure 1).

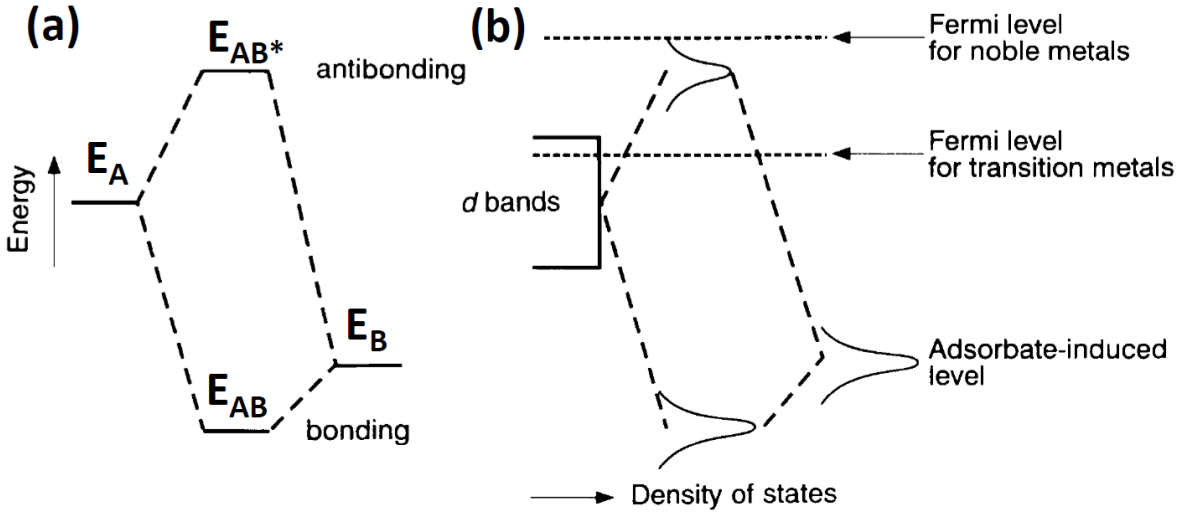

Figure 2. (a): In the linear combination of atomic orbitals (LCAO) approach, the chemical bond between atoms A and B originates via the overlap of the atomic orbitals (AO) Ψ_A and Ψ_B (having eigenvalues E_A and E_B, respectively), resulting in the formation of bonding (Ψ_{AB}) and antibonding (Ψ_{AB*}) molecular orbitals (MO), having eigenvalues E_{AB} and E_{AB*}, respectively) (b): Illustration of orbital levels of an adsorbate on a transition metal. Attractive bonding occurs when anti-bonding states are pushed above the Fermi level. XA probes such levels, XE the filled density of states. Unpublished figure, inspired from Ref.[41]

Palladium is the catalyst of choice for many hydrogenation reactions.[42,43] It is the most-active metal and still affords high selectivity. It is commercially used in the semi-hydrogenation of acetylenes.[44] Poly-olefins are plastics that find widespread application and polyethylene is probably the best-known polymer. Its synthesis requires streams of ethylene that are free of acetylenes, because these cause branching of the polymer chains degrading the polyethylene quality.[45] Catalytic hydrogenation of the triple bond to the olefin is the preferred catalytic route to achieve this. Over-hydrogenation must be prevented, however this is difficult, because a catalyst active in hydrogenation of triple bonds generally also catalyzes hydrogenation of the double bond, leading to loss of yield. As the goal is to diminish the concentration of acetylenes to extremely low values, the catalyst must be extremely selective to reacting the minority component in the reaction mixture. Preferred adsorption of the acetylene above olefin is an essential requirement to achieve this. Because of the stronger bonding, the catalyst surface is covered with acetylenes, which are the first ones to become hydrogenated. Hydrogen dissociative adsorption is a fundamental step in this reaction, which readily occurs on the palladium surface. Hydrogen atoms may remain at the surface or they may penetrate into the bulk forming palladium hydride.[46-51] As palladium may also form carbide by breaking of carbon - carbon bonds, the catalyst structure may be metallic, a hydride, or a carbide, depending on the conditions.[51-54]

EXAFS and XANES respectively at the Pd K and L_3 edges yield structural information about the formation of hydrides and carbides in supported palladium catalysts. L_3 edge XANES detects the empty d-DOS, and thus probes the palladium-hydrogen antibonding state.[46,48] Because the reactivity of surface and bulk hydrogen is different;[55] hydrides are suggested to be responsible

for the complete unselective hydrogenation, distinction between surface adsorbed and bulk absorbed hydrogen is needed. A different location of hydrogen on or in the particle leads to different bonding and electronic structure, which can be detected as shown below. EXAFS is a selective measure of the palladium - palladium bond length. Because hydrogen is too light to be detected directly, EXAFS is only sensitive to hydrogen ab- and adsorption via changes in the bond length, which can also be detected in diffraction.[51,56] Figure 3 shows in situ Pd L_3 XANES of alumina- and silica-supported palladium catalysts in which the palladium particle sizes vary between 1.3 to 10.5 nm. The spectra in the absence of hydrogen show minor differences (Figure 3a): the maximum intensity of the white-line (first resonance after the edge) is lowered with respect to the palladium bulk case (full line) and there is a slight positive shift with decreasing particle size. These changes originate from the different electronic structure in the nano-sized particles. Under one bar hydrogen at 300 K, the spectrum of the largest particles (10.5 nm) shows significant loss of intensity of the white-line and a major peak at about 8 eV above the absorption edge. The intensity of this peak is significantly lower in the spectra of catalysts with particles of 2.8 and 1.3 nm, respectively. In addition, the white-line in these latter spectra is significantly broadened at the high-energy side. These differences in spectra of catalysts with small respectively large palladium particles indicate that under hydrogen they adapt to different structures, which can be quantified by theoretical simulations. As mentioned above, the L_3 edge probes the empty d-DOS and is thus sensitive to the d-component in the anti-bonding state between palladium and hydrogen.

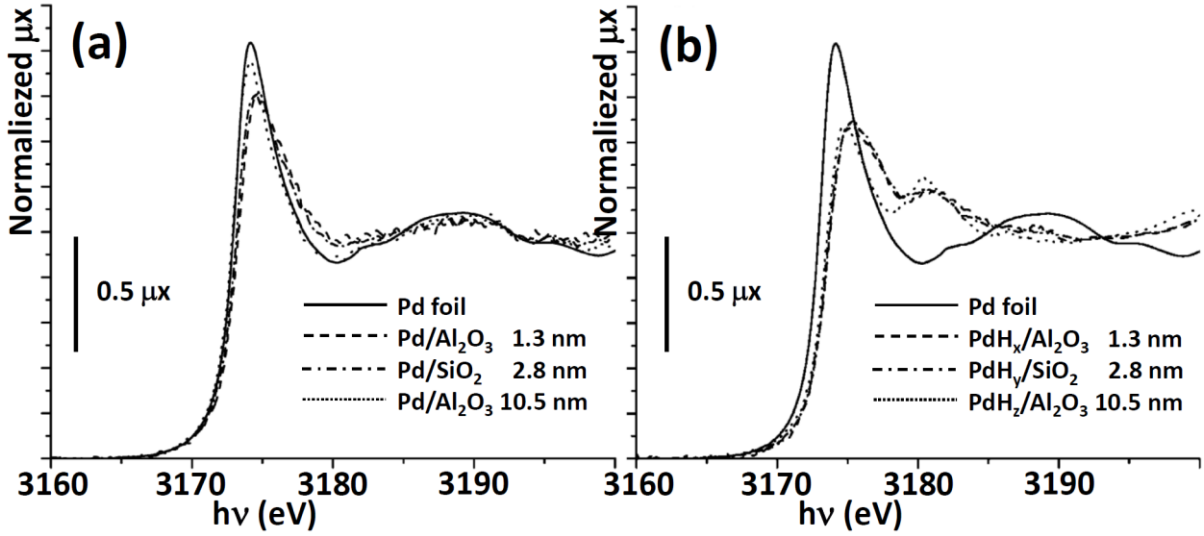

Figure 3. (a): Pd L_3 edge XANES of supported palladium nano-particles of different average size (1.3 nm dash; 2.8 nm dash-dot; 10.5 nm dot; bulk solid). (b): Pd L_3 edge XANES of the same particles after exposure to one bar hydrogen at 300 K; the spectrum of palladium foil is added as reference (solid curve). Adapted with permission from,[48] copyright ACS 2009.

XANES spectra can nowadays be successfully simulated with theoretical codes.[33,57,58] Figure 4 shows the effects of hydrogen adsorption both on the surface and into the bulk on the computed Pd L_3 edges XANES spectra (right ordinate axis) and DOS (left ordinate axis). Figure 4a shows the calculated density of states of bare palladium s (black), p (red), and d (blue), in addition to the L_3 XANES for a 13-atom palladium cluster (bold black). There is a close resemblance between the d density of states and the L_3 XANES, notably in the white-line region. Figure 4b illustrates the density of states of hydrogen s (green) and palladium d (blue) in addition to simulated L_3 XANES of a palladium hydride cluster of 27 atoms ($PdH_6Pd_{12}H_8$) (bold black).

Again, the d density of states is at the origin of the L_3 edge spectrum. The overlap of Pd(d) and H(s) illustrates the palladium-hydrogen anti-bonding nature of the 8 eV peak. Figure 4c overplots the H(s) (green) and Pd(d) (blue) with simulated L_3 XANES (black) of a $Pd_{13}H_8$ cluster with hydrogen exclusively at its surface. Mixing between Pd(d) and H(s) orbitals is at the origin of the broadening of the white-line in the L_3 edge XANES.[48]

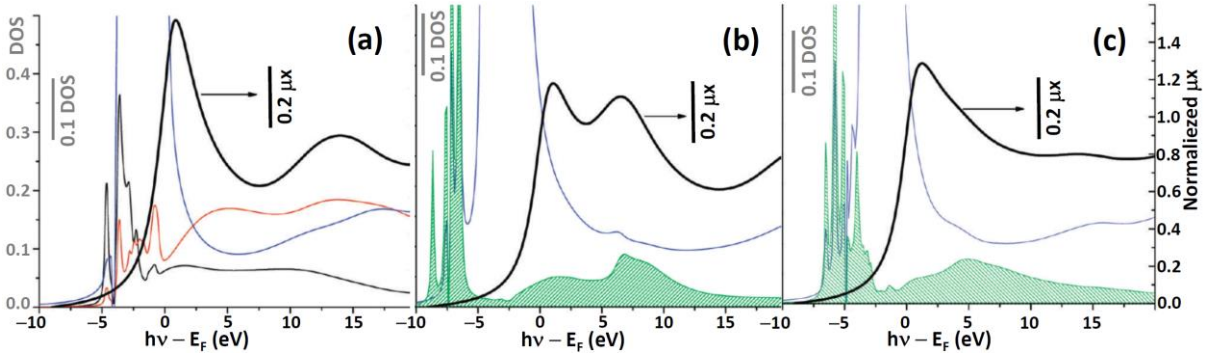

Figure 4. (a): Calculated density of states (DOS, left ordinate axis) of Pd(s) (black), Pd(p) (red), and Pd(d) (blue) overplotted with calculated Pd-L_3 XANES for Pd cluster of 13 atoms ($PdPd_{12}$) (bold black, right ordinate axis). (b): H(s) (green) and Pd(d) (blue) overplotted with calculated Pd-L_3 XANES for palladium hydride of 27 atoms ($PdH_6Pd_{12}H_8$) (bold black). (c): H(s) (green) and Pd(d) (blue) overplotted with calculated Pd-L_3 XANES for Pd_$Pd_{12}H_8$ with the surface palladium atom set as absorbing atom (bold black). Adapted with permission from,[48] copyright ACS 2009.

These spectra simulations help to interpret the experimental ones: Bulk hydride formation occurs readily in the larger particles (>10 nm), whereas the extend of hydride formation is significantly less in particles of 1.3 and 2.8 nm. Nonetheless, hydrogen absorption into the core of even the smallest particles occurs. In addition, the significant broadening of the white-line is proof of the existence of surface-adsorbed hydrogen in these smaller particles. This study shows how XANES is a very sensitive tool to detect the local structure of the site that adsorbs reactants and intermediates. [48,59-61]

4.2. Direct detection of valence structure by x-ray emission

Valence electrons are involved in the bonding between atoms. Mixing between orbitals on the atoms that are involved in the bonding occurs by forming bonding and anti-bonding orbitals (Figure 2a). The overlap and mixing between the atomic orbitals of atoms yield molecular orbitals, whereas in bulk metals, the atomic orbitals are hybridized into bands, which can overlap and mix with atomic orbitals of adsorbed species to form bonds. Bonding only occurs in case the bonding orbitals are filled and the anti-bonding ones are -at least partially- pushed above the Fermi level (Figure 2b).[41] As illustrated in the case of hydrogen on (and in) palladium particles (see above section 4.1), the empty anti-bonding states can be probed in XANES spectra, permitted that the correct orbitals, thus absorption edge(s), are probed. Probing empty density of states by measuring XA is widespread and has been exercised since decades. Probing the energy structure of the valence electrons is possible in in XE, but it is much more experimentally demanding, because of the low probability of core hole annihilation by an electron from the valence shell, yielding extremely low count rates. High flux beam lines and sensitive detectors are nowadays available, and such measurements are becoming routine and fast measurements have been achieved.[62] The first example of detection of the valence band of a 5d metal catalyst through valence to core XE, is that of supported platinum nano-sized particles.[63] The experiment illustrates how the energy structure of the d-band can be made visible and how it changes upon the adsorption of carbon monoxide. Figure 5 shows the

transitions that are probed in the experiment. A Pt 2p electron is excited into empty 5d density of states; this is the XA process. Detection of the valence to core emission in an energy-dispersive manner yields the XE (Figure 1b). Plotting the x-ray emission intensity as function of the energies of both incident (hν) and emitted (hν') the photon energies yields a two-dimensional plot, the RIXS plane, standing for resonance inelastic x-ray scattering. The high-brilliance beam line ID26 at the ESRF and its Johanson-type high energy emission spectrometer were used for this experiment. From these planes, the Pt(5d) band can be visualized. The 5d-band of the one nanometer-sized platinum particles free of any adsorbate extended to the Fermi level (Figure 6), indicative of metallic character. The adsorption of carbon monoxide shifted the band downward in energy and opened up a band gap. Thus, depending on the kind -and amount- of adsorbate, strong changes in electronic structure occur, which are reminiscent of the bonding. Figure 2 showed that upon adsorption of a species on the surface of a metal, bonding and anti-bonding states form. In addition, such bonding is, as shown in case of carbon monoxide, associated with a downward shift of the whole Pt(5d) band. Such downward shift makes the Pt(5d) electrons less prone to bond adsorbates as the anti-bonding orbitals are located at lower energy, decreasing the tendency to form bonds.

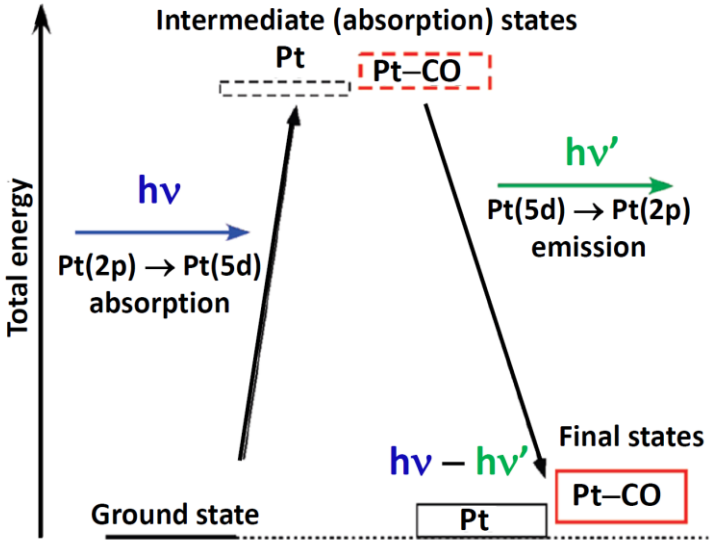

Figure 5. Scheme of electron transitions in a resonance inelastic x-ray scattering (RIXS), experiment. Adapted with permission from ref.[63], copyright ACS 2010.

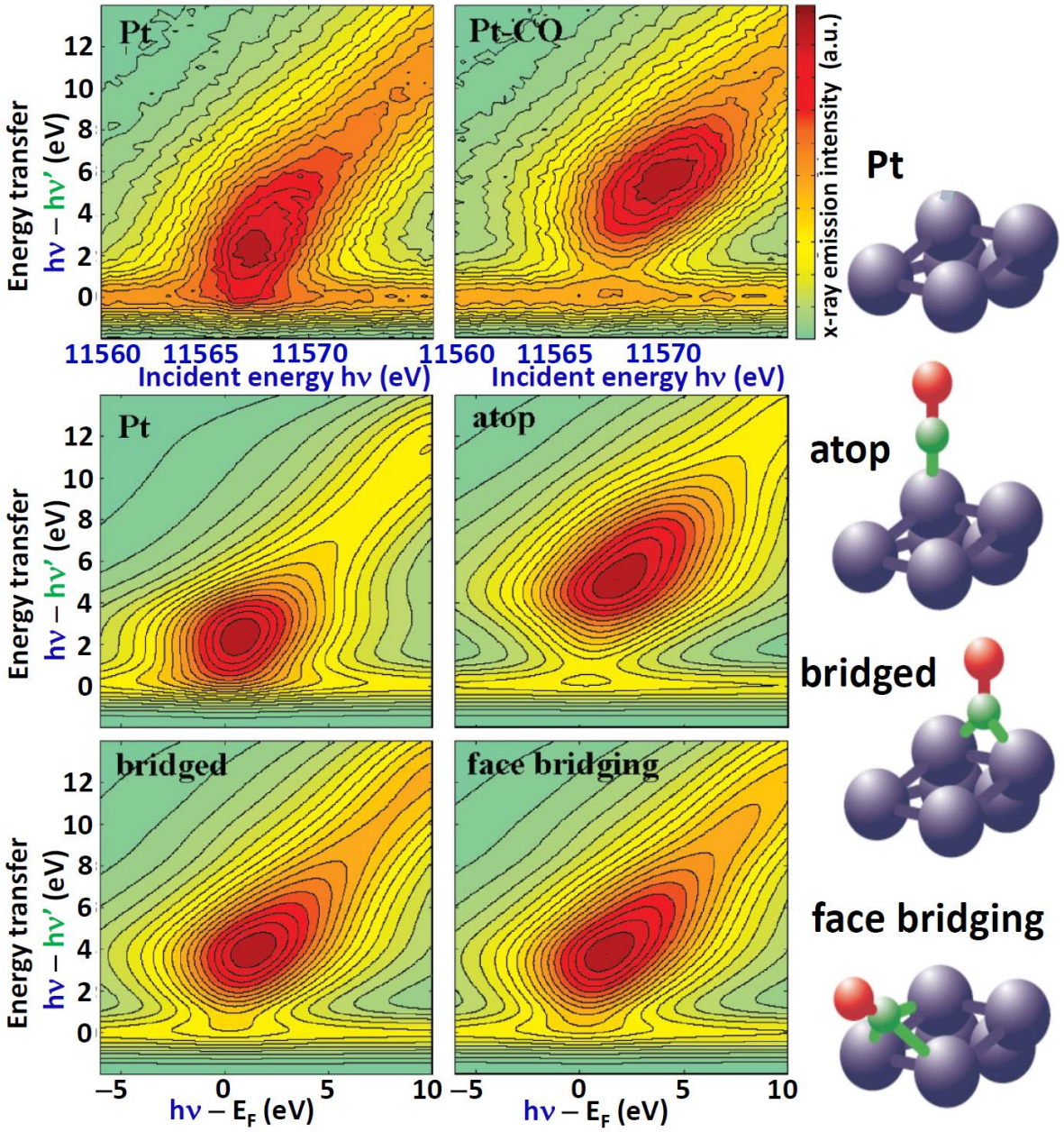

Figure 6. Valence to core RIXS planes of platinum nanoparticles in absence and presence of carbon monoxide on their surface. Upon carbon monoxide adsorption, the Pt(5d) band moves away from the Fermi level (E_F) expressed by a larger energy transfer of the center of mass of the feature. Top two panels report the experimental data, the bottom four the theoretically simulated spectra of a bare particle and three with carbon monoxide adsorbed on distinct sites, as depicted in the clusters reported in the right part (Pt, C and O atoms are reported as gray, green and red spheres, respectively). Adapted with permission from ref.[63], copyright ACS 2010.

4.3. From spectator to active species: time resolved in situ and operando spectroscopy on a ceria-based oxidation catalyst

The catalytic action can be described as a cycle, in which one or more reactants adsorb onto the catalyst surface, then react -often in multiple steps- and subsequently desorb to free the catalyst surface to complete the cycle.[7,64] This process is associated with a dynamic structure change of the active site.[65] The bond that is formed between reactant and catalyst surface can be very strong, from tens to over hundreds of kJ/mol. To enable the bond formation, the local structure of the active site changes and one or more atoms may change oxidation state and/or local

structure. Oxidation reactions require activation of the oxygen molecule, which leads to a change in oxidation state of the metal atom(s) that bond(s) the oxygen species (vide supra).[64,66-69] In hydrogenation reactions, for example on nano-sized metal particles, the dissociative adsorption of hydrogen leads to atomically adsorbed hydrogen, which increases the metal-metal bond length within the nano-particle,[49,51] because of the charge transfer that occurs.[70] For the metal-hydrogen bond to form, its strength must roughly be in access of half the bond strength in molecular hydrogen, which is about 420 kJ/mol. Overall, within one catalytic cycle, the catalyst structure undergoes various structural changes. In order to capture such change, the measurement of catalyst structure before and after the catalytic action is insufficient and to determine the structure of an active catalyst is generally done best under catalytic conditions: In situ or operando measurements are essential, however, not necessarily sufficient. The structure that is measured under such conditions captures the catalyst structure, which is determined by the slowest step in the overall reaction. It does not capture the nature and dynamics of the structural changes that occur during a catalytic cycle. Knowledge of the reaction mechanism and measuring the individual reaction steps are thus essential in understanding the relation between structure and performance.[64,66]

X-ray spectroscopy is a quantitative method and it captures the structure of all atoms in an element-specific manner. The benefit is that there are no undetected species, provided their concentration is sufficiently high to be detected. The disadvantage is that many of the detected atoms may not contribute to the catalytic active cycle and be spectator species, which may dominate the signal. There exist various methods to distinguish between spectator and active species. Steady state transient kinetic analysis (SSITKA) enables measuring the time-resolved change of isotopologue concentration after a switch of one or more reactants to an isotopologue.[71] Thus, there is minimal impact on the reaction conditions and mechanism and one is able to relate the changes in a time-resolved manner to steady state kinetic parameters. Vibrational spectroscopy has adopted such methods and transient ones with a focus to identify active adsorbed species and intermediates.[15,72,73]

Measuring the structural response after applying a change to the system, such as the change of concentration of one of the reactants yields information about the ensemble of atoms that is involved in the catalytic cycle: the structural response of these atoms is correlated to the catalytic reaction, the response of spectator species has no direct relationship.[74-76] Time-resolved measurements are essential and recent advances in time-resolved x-ray-based spectroscopy enable such measurements.[77,78]

A much-investigated reaction is the oxidation of carbon monoxide over noble metals. It is relevant in exhaust gas treatment and one of the most-studied model reactions in catalysis. Low temperature carbon monoxide oxidation is characterized by adsorption of carbon monoxide on the metal particle, which prevents the oxygen from reacting to the metal surface.[79] After desorption of carbon monoxide, gas phase oxygen and carbon monoxide compete for the freed surface. After oxygen adsorption, it may react to an adsorbed carbon monoxide. In automotive exhaust catalysts, ceria is present as a dopant, because it stabilizes nano-sized metal particles[80,81] and it enhances the rate of reaction. In the oxide, the cerium atom has an oxidation state of +IV, which can undergo a reversible redox reaction to the +III state. During this cycle, oxygen is released and take up again (Figure 7a). Such oxygen storage capacity is often invoked in catalysis and Ce^{3+} is related to catalytic activity.

To distinguish spectator species from catalytic-relevant ones, a transient experiment was designed,[76] in which the concentration of reactants was rapidly changed and the structural response of the catalyst determined. At first the catalyst structure was measured under steady state conversion, thus in the presence of carbon monoxide and oxygen. Under the condition, the

conversion level of carbon monoxide was below 10%. The structural response was measured in a time-resolved manner after rapidly switching off the oxygen supply.
X-ray emission spectroscopy is sensitive to the local structure and oxidation state and can be performed in a time-resolved manner (Figure 7b-e).[78] The method that yielded the highest sensitivity to the cerium oxidation state was resonant XES, in which an electron is excited into the absorption edge of the conduction band and the resulting x-ray fluorescence is selectively measured (Figure 1b). The relatively weak fluorescent signal requires repetition of the experiment, thus multiple switches in gas concentration. A requirement for such measurement is that the structural and electronic changes are fully reproducible.

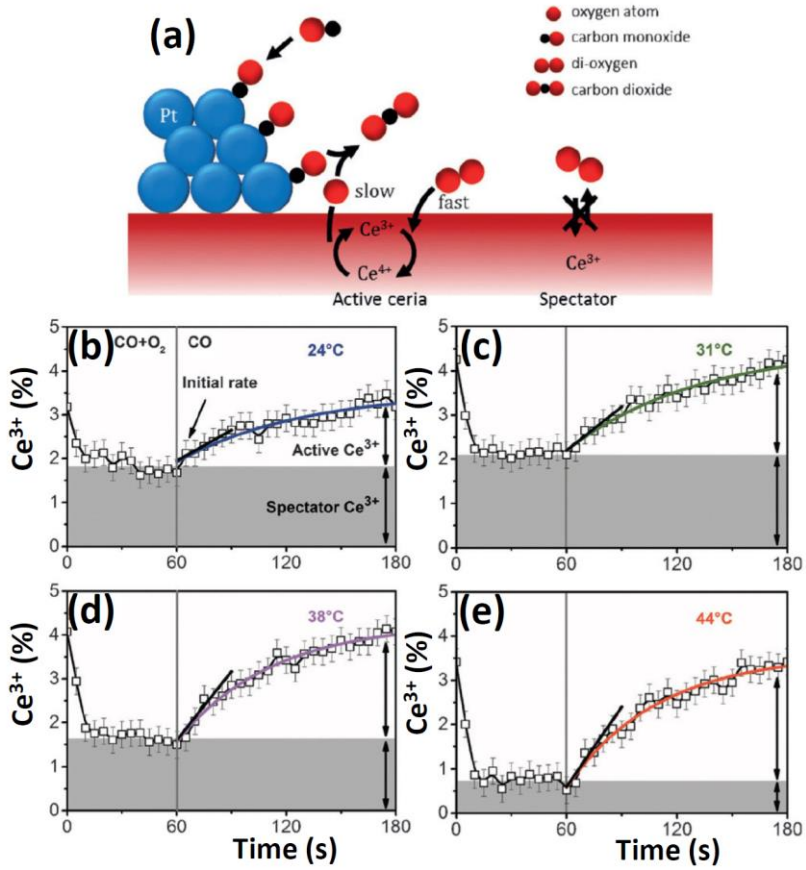

Figure 7. (a) Representation of oxygen uptake and release by ceria during the carbon monoxide oxidation cycle on a Pt/CeO_2 catalyst. In the slow part of the cycle, an oxygen atom from ceria at the $Pt–CeO_2$ interface reacts with carbon monoxide adsorbed on platinum to afford carbon dioxide, an oxygen vacancy, and two Ce^{3+} species. The fast part of the cycle involves carbon monoxide readsorption on platinum and oxygen activation on ceria resulting in healing of the oxygen vacancy and oxidation of active Ce^{3+} species. Ce^{3+} spectator species do not participate in carbon monoxide oxidation. (b–e) Transient Ce^{3+} concentrations in the Pt/CeO_2 catalyst measured with RXES during cycling between 1% CO+4% O_2 (0–60 s) and 1% CO (60–180 s) gas mixtures at 24, 31, 38, and 44 °C. The increase in Ce^{3+} concentration in 1% CO was fitted by an exponent function and the initial rate at the moment of switch (60 s) was determined (indicated as the slope). The concentrations of active and spectator Ce^{3+} species are indicated by arrows. Reproduced with permission from ref., [76] copyright Wiley VCH 2015.

Figure 7b-e shows the concentration of Ce^{3+} in the catalyst under the different conditions. At 24 °C (Figure 7b) under steady state conditions, about 2% of the cerium atoms had an oxidation state of III. Upon switching to a feed with only carbon monoxide an increase in its concentration was observed, most rapidly in the beginning. The switch back to steady state catalytic conditions led to a very rapid re-oxidation and re-establishing of the original Ce^{3+} concentration. Thus, there is a steady state concentration of Ce^{3+} and a fraction that changes its

oxidation state upon switching. Repeating the same switching experiment at higher temperature (Figure 7c-e) led to a gradual decrease in the steady-state concentration of Ce^{3+} and to a more rapid initial formation of 'reversible' Ce^{3+}. The amount of redox-active cerium increased with temperature. Determining the initial rates of cerium reduction and comparing this to the steady state carbon monoxide rates of reaction yielded very similar values, differing by about a factor of two at most, after correction for stoichiometry.[76] This indicates that cerium reduction and re-oxidation is involved in the catalytic cycle and participate in the oxygen activation: the steady state conversion and the cerium reduction process are kinetically coupled. Because Ce^{3+} re-oxidation is very rapid, its concentration under steady-state conditions is very small. The Ce^{3+} that is detected under steady state conditions is not participating in the reaction, but is a spectator species. Its concentration changes over time, but at a much slower time-scale than relevant to the conversion in the catalytic cycle. The Ce^{3+} that is measured under steady state conditions in the true operando experiment is not relevant to the catalytic conversion; the Ce^{3+} that is involved in the catalytic cycle is short-lived and its concentration under steady-state conditions very low and difficult to detect.
The factors that made this experiment successful were the high sensitivity of the method to small concentrations of Ce^{3+} and the ability to measure its changes in a time-resolved manner. The experiment illustrates how the atoms that form the catalytically active site may be difficult to be detected and that they can remain invisible even in true in situ and operando experiments. Time resolved measurements of transient experiments help to resolve this. X-ray spectroscopy is one of the methods that provides the required time resolution. The example given here is based on XES, however, XANES and EXAFS can also be applied, like many other characterization techniques. Which is the method of choice depends on the kind of information and time-resolution that are required. With respect to x-rays, developments in providing x-ray pulses of higher brilliance and new and improved detectors have made measurements in the time-domain possible. These developments will continue, and enable measuring smaller fractions, well below one percentage, and at much faster rates. The milli-, micro-, nano-, pico-, and femto-second time regimes are all becoming readily accessible.[77,78,82-85]

4.4. Red-ox chemistry of UiO-67-Cu MOF followed by in situ EXAFS and XANES

Metal-organic Frameworks (MOFs) are defined as porous, crystalline materials composed by metal-based cornerstones (metal ions or clusters) connected by organic linkers[86-89] to form a three-dimensionally ordered framework. Due to their high surface area, and enormous structural and compositional flexibility, these micro-porous materials have attracted in the last decade a paramount interest. Heterogeneous catalysis is among the most promising application fields of MOFs.[90-96] On the one hand, the flexibility in synthesis of different MOFs topologies (much larger than that of zeolites) makes this class of materials ideal to synthesize new catalysts with unique properties such as shape-selectivy. On the other hand, the insertion of a given metalorganic complex, active in homogeneous catalysis, as metallic cornerstone in a new MOF framework represents an attractive way to heterogenize a homogeneous system. The main drawback in the use of MOFs as heterogeneous catalyst, is their poor thermal stability (much lower than that of zeolites), limiting the application to reaction running at mild conditions, even though a limited amount of structures show high stability.
Due to their outstanding stability at high temperatures, high pressures and resistance in presence of different solvents, the UiO-66, -67 and -68 classes of iso-structural MOFs,[97-102] discovered at the Oslo University, are among the few MOFs already commercialized for applications in the fields of catalysis, H_2 storage, and gas purification. They are obtained by connecting $Zr_6O_4(OH)_4$ inorganic cornerstones with 1,4-benzene-dicarboxylate, 4,4′biphenyl-

dicarboxylate and 4,4′-terphenyl-dicarboxylate linkers, for the UiO-66, -67 and -68 MOFs, respectively.[97]

The outstanding properties of the UiO-66/68-family MOFs make them an ideal test-bench to explore post-synthesis functionalization approaches,[103-106] aiming to insert catalytically active sites inside the MOFs frameworks. As an example, a small fraction of the linkers in the UiO-67 MOF can be replaced by moieties exhibiting metal-chelating ability, such as bipyridine-dicarboxylate (bpydc), enabling the grafting of metal ions, while retaining the exceptional thermal and hydrothermal stability of the parent MOF. With this respect, the Oslo group has recently synthesized by different routes proof-of-concept platinum-functionalized UiO-67 derivatives.[106] In situ and operando Pt L_3-edge XAS experiments were used to thoroughly characterize these materials and the rich reactivity in the local environment of the platinum centers. Pt(II) complexes grafted to the MOF framework via the bpydc linker can be reduced to bpydcPt(0) sites under hydrogen flow between 600 and 700 K, as probed by a sophisticated parametric analysis of temperature-dependent EXAFS data, or they can be oxidized at room temperature to Pt(IV) through oxidative addition of bromine from the liquid phase. The large pore size of UiO-67 also allows for ligand exchange between 2 Cl^- and even bulky ligands such as toluene-3,4-dithiol.[106,107] These studies pave the way to the exploration of a novel class of metal-functionalized MOFs, representing attractive candidates for industrial applications aiming to heterogenization of homogeneous catalytic reactions, with the advantages of recyclability and efficient catalyst/product separation. The same group succeeded in the synthesis of the Rh- and Ir- and Cu-UiO-67 analogues.[108,109]

The combination of XANES, EXAFS and FTIR spectroscopies, applied under in situ and operando conditions, was applied by Braglia et al.[109] to verify the successful incorporation of copper ions in bpydc-containing UiO-67 MOFs. The authors observed isolated copper-sites grafted to the MOF framework *via* coordination to the two nitrogen atoms of the bpydc unit, without any evidence of metal clusters formation.[109] On the basis of DFT-assisted EXAFS fitting, the authors identified the other ligands in the copper-coordination sphere, while the changes in the copper oxidation state was followed by XANES. In particular, EXAFS data for the as-prepared materials (collected at room temperature in air) are consistent with [Cu(II)(bpydc)(OH)Cl] species (Figure 8a-c). The negatively-charged OH^- group is then released upon heating at 523 K under nitrogen-flux, triggering a reduction of the original four-coordinated Cu(II) sites to three-coordinate Cu(I) species, [Cu(I)(bpydc)Cl], while preserving coordination to the UiO-67 framework by the chelating bpydc linker (Figure 8d-f). Further insights in the nature and reactivity of these [Cu(I)(bpydc)Cl] complexes, representing an interesting platform for future experiments on Cu(I)-catalyzed reactions, were achieved by monitoring with EXAFS, XANES and FTIR the interaction of the thermally-treated material with carbon monoxide as probe molecule. The three techniques pointed out the efficient and reversible formation [Cu(I)(bpydc)(CO)Cl] species as highlighted by the EXAFS fit reported in Figure 8g-i.

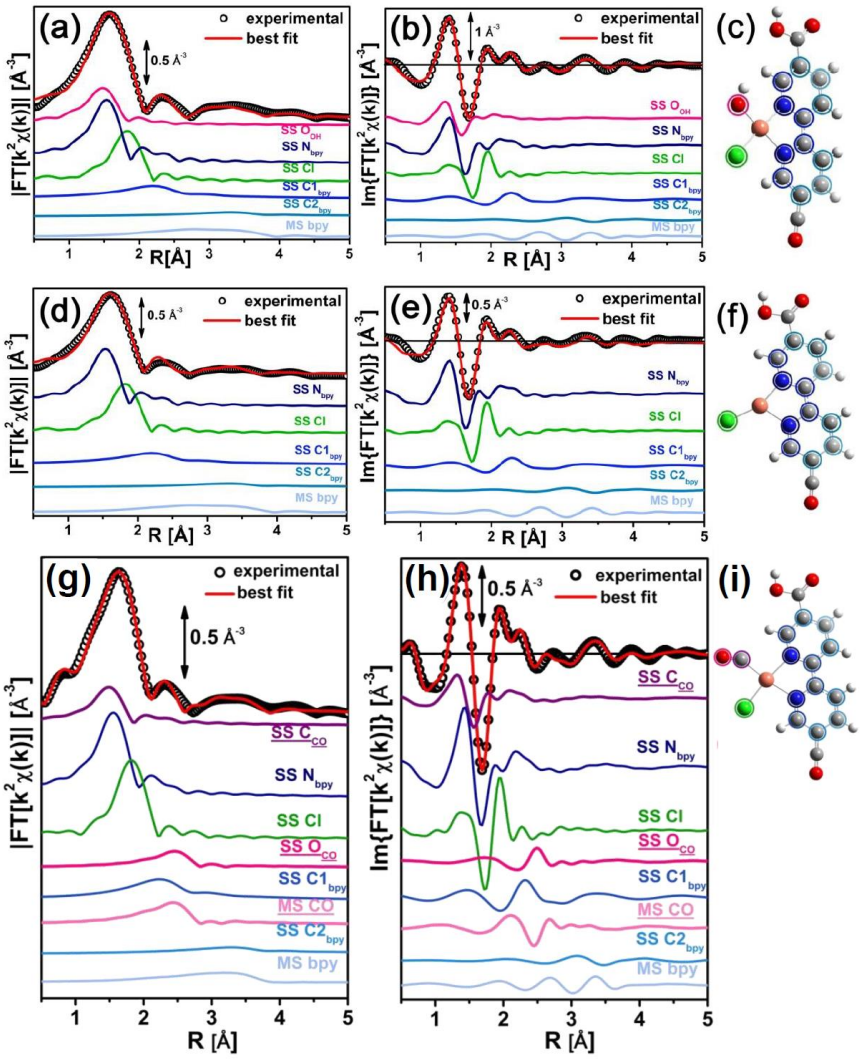

Figure 8. Parts (a,b): modulus (a) and imaginary part (b) of the experimental and best fit FT EXAFS spectra for Cu-UiO-67 in the as-prepared state (at RT, in air). The experimental data are shown as black dots and the best fit with red solid line. Moreover, the single scattering (SS) contribution involving the N(bpy), Cl, O(OH), C1(bpy) and C2(bpy) atomic neighbors as well as the multiple scattering (MS) involving the atoms of the bpy unit are reported. Part (c): DFT-optimized structure used as starting point for the EXAFS fit. Atom color code: Cu: orange; O: red; N: blue; Cl: green, C: gray; H: white. Parts (d, e, f): as parts (a, b, c) for the UiO-67-10%bpy-Cu(I) sample measured at RT after thermal treatment at 523 K under nitrogen. Parts (g, h, i): as parts (a, b, c) after successive interaction with carbon monoxide at 300 K. In parts (c, f, i), circled atoms are those included in the EXAFS fit and the color of the circle is the same used in parts (a, b, d, e, g, h) for the lines of the corresponding SS paths. Reproduced with permission from ref.,[109] copyright Elsevier 2016.

The overall picture obtained after the EXAFS data analysis (Figure 8), is confirmed by XANES simulations performed with the accelerated version of the FDMNES code [58,110] starting from the DFT-optimized geometries (Figure 8c,f,i). Figure 9a,b shows the experimental and theoretical XANES spectra for the key states of Cu-UiO-67-discussed above: as-prepared material in air (black), after thermal treatment at 523 K in nitrogen (red) and after interaction with carbon monoxide (blue). In the three cases, the intensity of the white line well reproduced the changes observed in the experimental spectra. Indeed, the spectrum simulated using the [Cu(bpydc)(OH)Cl] model presents an intense white-line peak, as observed for as-prepared MOFs in air. The white-line peak decreases during thermal treatment in nitrogen and it remains almost unchanged upon carbon monoxide adsorption, as also found in the simulated spectra for [Cu(bpydc)Cl] and [Cu(bpydc)(CO)Cl] models. The energy of the absorption threshold in the

simulated spectra qualitatively reproduces the experimental tendency. The position of the threshold obtained for the [Cu(bpydc)(OH)Cl] model is located at higher energy, as observed for the as-prepared MOF in air. Conversely, in the theoretical spectra corresponding to [Cu(bpydc)Cl] and [Cu(bpydc)(CO)Cl] species, the absorption threshold shifts at lower energy, in agreement with the experimental evidences for dominant Cu(I) sites after thermal treatment and interaction with carbon monoxide. The agreement between theory and experiment can be better appreciated in Figure 9c-d reporting the difference XANES spectra showing the effect of -OH removal and copper reduction (part c) and of carbon monoxide adsorption (part d). The difference XANES method (also known as ΔXANES),[59,111] represents an accurate way to better appreciate small difference in XANES spectra upon perturbation of the system under investigation. The theory is perfectly able to reproduce the difference observed during the activation process (Figure 9c), while a less quantitative agreement between theory and experiment is observed upon carbon monoxide adsorption; however, qualitatively the theory correctly predicts a negative Δμx curve in the (8980-8990) eV range, followed by a positive region, that subsequently decreases in intensity.

The trend of the charge on copper-site confirmed the results obtained by XANES qualitative analysis and EXAFS fits: the metal starts from a local charge of 1.8 |*e*| (≈ 2 |*e*|) for the [Cu(bpydc)(OH)Cl] complex, representative of the as-prepared sample. For the [Cu(bpydc)Cl] complex, modeling the thermally-treated material, the charge on copper is reduced to 1.1 |*e*| (≈ 1 |*e*|). Conversely, the coordination of a carbon monoixde molecule on Cu(I) sites, [Cu(bpydc)(CO)Cl] model, slightly increases the local charge on copper to 1.4 |*e*|, although being still significantly lower with respect to what found for the [Cu(bpydc)(OH)Cl] case. The calculated local charge on copper for the different models qualitatively confirms the experimental observations: Cu(II) centers grafted to the bpydc linker in the as-prepared MOFs, mostly reduced to Cu(I) in nitrogen at 523 K. Theoretical modeling suggests that carbon monoxide coordination leads to a small alteration of local charge around Cu(I), albeit the calculated value of 1.4 |*e*| is still compatible with a formal +1 oxidation state of the metal center.

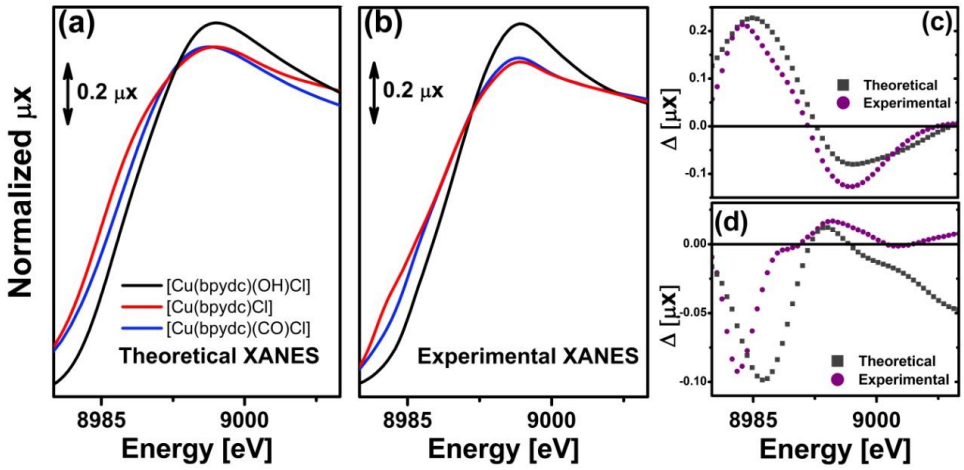

Figure 9. (a): Cu K-edge theoretical XANES spectra calculated with FDMNES code [58,110] from DFT-optimized geometries of [Cu(bpydc)(OH)Cl] (black curve), [Cu(bpydc)Cl] (red curve) and [Cu(bpydc)(CO)Cl] (blue curve), representative of the Cu-UiO-67-10%bpy sample in the different experimental conditions. (b): (a) for the corresponding experimental spectra collected on Cu-UiO-67-10%bpy sample at RT; same color code. (c): comparison between the experimental (scattered purple circles) and theoretical (scattered gray squares) difference XANES spectra showing the effect of reduction via thermal treatment: [Cu(bpydc)Cl] – [Cu(bpydc)(OH)Cl]. Part (d): as part (c) for the difference XANES spectra showing the effect of carbon monoxide adsorption on the thermally-treated sample: [Cu(bpydc)(CO)Cl] – [Cu(bpydc)Cl]. Reproduced with permission from ref.,[109] copyright Elsevier 2016.

These results lay the foundations for future operando studies aiming to characterize in more detail the redox behavior of the grafted copper-sites, by exposing the thermally-treated samples to both reducing (for example under hydrogen), and oxidizing conditions (under oxygen).

5. Conclusions

After having introduced the basic theoretical background of XAS (both XANES and EXAFS) and XES (both resonant and non-resonant) spectroscopies, we selected four examples where XAS and/or XES were relevant in understanding the local structure and the electronic configuration of active centers in heterogeneous catalysts. In situ and operando conditions are essential to capture catalytically relevant structures. Time resolution in transient experiments helps to distinguish spectator species from the catalytically active ones. Although x-ray spectroscopy is used in catalysis since many decades, rapid method development opens new opportunities and avenues for catalyst characterization and identification of the catalytically active site. The combination with complementary tools is essential to fully comprehend any catalytic system.

Acknowledgments

C. Lamberti, acknowledges the Megagrant of the Russian Federation Government to support scientific research at the Southern Federal University, no. 14.Y26.31.0001.

References

1. Clausen B. S., Steffensen G., Fabius B. et al (1991) Insitu cell for combined XRD and online catalysis tests - studies of Cu-based water gas shift and methanol catalysts. *J. Catal.*, **132**, 524-535.
2. Couves J. W., Thomas J. M., Waller D. et al (1991) Tracing the conversion of aurichalcite to a copper catalyst by combined X-ray absorption and diffraction. *Nature*, **354**, 465-468.
3. Bordiga S., Groppo E., Agostini G. et al (2013) Reactivity of surface species in heterogeneous catalysts probed by in situ X-ray absorption techniques. *Chem. Rev.*, **113**, 1736-1850.
4. Glatzel P., Bergmann U. (2005) High resolution 1s core hole X-ray spectroscopy in 3d transition metal complexes - electronic and structural information. *Coord. Chem. Rev.*, **249**, 65-95.
5. Singh J., Lamberti C., van Bokhoven J. A. (2010) Advanced X-ray absorption and emission spectroscopy: in situ catalytic studies. *Chem. Soc. Rev.*, **39**, 4754-4766.
6. Bai R. P., Zhang G. H., Yi H. et al (2014) Cu(II)-Cu(I) Synergistic Cooperation to Lead the Alkyne C-H Activation. *J. Am. Chem. Soc.*, **136**, 16760-16763.
7. Bonino F., Groppo E., Prestipino C. et al (2015) Catalyst Characterization by XAS and XES Spectroscopies: In Situ and Operando Experiments. In Mobilio S., Boscherini F., and Meneghini C. (eds), Synchrotron Radiation: Basics, Methods and Applications, Springer Berlin Heidelberg, Berlin, Heidelberg, pp. 717-736.
8. Lamberti C., van Bokhoven J. A. (2016) X-Ray Absorption and Emission Spectroscopy for Catalysis. In van Bokhoven J. A. and Lamberti C. (eds), X-Ray Absorption and X-Ray Emission Spectroscopy: Theory and Applications, John Wiley & Sons, Chichester (UK), pp. 353-383.
9. Tromp M. (2015) Catalysis seen in action. *Philos. Trans. R. Soc. A-Math. Phys. Eng. Sci.*, **373**, 12.
10. Makosch M., Kartusch C., Sa J. et al (2012) HERFD XAS/ATR-FTIR batch reactor cell. *Phys. Chem. Chem. Phys.*, **14**, 2164-2170.
11. Makosch M., Sa J., Kartusch C. et al (2012) Hydrogenation of Nitrobenzene Over Au/MeOx CatalystsuA Matter of the Support. *ChemCatChem*, **4**, 59-63.
12. Meunier F. C. (2010) The design and testing of kinetically-appropriate operando spectroscopic cells for investigating heterogeneous catalytic reactions. *Chem. Soc. Rev.*, **39**, 4602-4614.
13. Agostini G., Gianolio D., Lamberti C. (2017) In situ and operando catalysis: instrumentation and experimental set-ups. In Chantler C. T., Bunker B., and Boscherini F. (eds), International Tables Volume I, 3.38, IUCr, pp. submitted.
14. Bordiga S., Bonino F., Lillerud K. P. et al (2010) X-ray absorption spectroscopies: useful tools to understand metallorganic frameworks structure and reactivity. *Chem. Soc. Rev.*, **39**, 4885-4927.

15. Bordiga S., Lamberti C., Bonino F. et al (2015) Probing zeolites by vibrational spectroscopies. *Chem. Soc. Rev.*, **44**, 7262-7341.
16. Lamberti C., Borfecchia E., van Bokhoven J. A. et al (2016) XAS Spectroscopy: Related Techniques and Combination with Other Spectroscopic and Scattering Methods. In van Bokhoven J. A. and Lamberti C. (eds), X-Ray Absorption and X-Ray Emission Spectroscopy: Theory and Applications, John Wiley & Sons, Chichester (UK), pp. 303-350.
17. Dirac P. A. M. (1927) The quantum theory of emission and absorption of radiation. *Proc. Roy. Soc. (London) A*, **114**, 243-265.
18. Fermi E., *Nuclear physics*, University of Chicago Press, Chicago, 1950.
19. Teo B. K., Joy D. C., *EXAFS spectroscopy: techniques and applications* Plenum, New York, 1981.
20. Boscherini F. (2008) X-ray absorption fine structure in the study of semiconductor heterostructures and nanostructures. In Lamberti C. (ed), Characterization of Semiconductor Heterostructures and Nanostructures, Elsevier, Amsterdam, pp. 289-330.
21. Borfecchia E., Gianolio D., Agostini G. et al (2013) Local and long order structural determination by combining EXAFS and diffraction techniques. In Llabrés i Xamena F. X. and Gascón J. (eds), Metal-Organic Frameworks in heterogeneous catalysis, RSC, Cambridge, pp. 143-208.
22. Dong C.-L., Guo J., Chen Y.-Y. et al (2007) Soft-x-ray spectroscopy probes nanomaterial-based devices. *SPIE Newsroom*, doi: 10.1117/1112.1200708.1200812.
23. Gel'mukhanov F., Agren H. (1999) Resonant X-ray Raman scattering. *Phys. Rep.-Rev. Sec. Phys. Lett.*, **312**, 87-330.
24. Glatzel P., Sikora M., Smolentsev G. et al (2009) Hard X-ray photon-in photon-out spectroscopy. *Catal. Today*, **145**, 294-299.
25. Bergmann U., Glatzel P. (2009) X-ray emission spectroscopy. *Photosynth. Res.*, **102**, 255-266.
26. Garino C., Borfecchia E., Gobetto R. et al (2014) Determination of the electronic and structural configuration of coordination compounds by synchrotron-radiation techniques. *Coord. Chem. Rev.*, **277-278**, 130-186.
27. Kotani A., Shin S. (2001) Resonant inelastic x-ray scattering spectra for electrons in solids. *Rev. Mod. Phys.*, **73**, 203-246.
28. Luches P., D'Addato S., Valeri S. et al (2004) X-ray absorption study at the Mg and O K-edges of ultrathin MgO epilayers on Ag(001). *Phys. Rev. B*, **69**, Art. n. 045412.
29. Sandstrom D. R., Lytle F. W. (1979) Developments in extended X-Ray absorption Fine structure applied to chemical systems. *Ann. Rev. Phys. Chem.*, **30**, 215-238.
30. Lee P. A., Citrin P. H., Eisenberger P. et al (1981) Extended x-ray absorption fine structure-its strengths and limitations as structural tool. *Rev. Mod. Phys.*, **53**, 769-806.
31. Filipponi A., Di Cicco A., Natoli C. R. (1995) X-ray-absorption spectroscopy and n-body distribution functions in condensed matter .1. Theory. *Phys. Rev. B*, **52**, 15122-15134.
32. Rehr J. J., Albers R. C. (2000) Theoretical approaches to x-ray absorption fine structure. *Rev. Mod. Phys.*, **72**, 621-654.
33. Kas J. J., Jorissen K., Rehr J. J. (2016) Real-Space Multiple-Scattering Theory of X-Ray Spectra. In van Bokhoven J. A. and Lamberti C. (eds), X-Ray Absorption and X-Ray Emission Spectroscopy: Theory and Applications, John Wiley & Sons, Chichester (UK), pp. 51-72.
34. Sayers D. E., Stern E. A., Lytle F. W. (1971) New technique for investigating noncrystalline structures: Fourier analysis of the extended x-ray absorption fine structure. *Phys. Rev. Lett.*, **27**, 1204-1207.
35. Stern E. A. (1974) Theory of the extended x-ray-absorption fine structure. *Phys. Rev. B*, **10**, 3027-3037.
36. Lytle F. W., Sayers D. E., Stern E. A. (1975) Extended x-ray-absorption fine-structure technique. II. Experimental practice and selected results. *Phys. Rev. B*, **11**, 4825-4835.
37. Lamberti C., Palomino G. T., Bordiga S. et al (2000) Structure of homoleptic $Cu^{I}(CO)_3$ cations in Cu^{I}-exchanged ZSM-5 zeolite: An X-ray absorption study. *Angew. Chem. Int. Edit.*, **39**, 2138-2141.
38. Groppo E., Prestipino C., Lamberti C. et al (2003) Growth of NiO on Ag(001): Atomic environment, strain, and interface relaxations studied by polarization dependent extended X-ray absorption fine structure. *J. Phys. Chem. B*, **107**, 4597-4606.
39. Lamberti C. (2004) The use of synchrotron radiation techniques in the characterization of strained semiconductor heterostructures and thin films. *Surf. Sci. Rep.*, **53**, 1-197.
40. Gianolio D., Groppo E., Vitillo J. G. et al (2010) Direct evidence of adsorption induced Cr^{II} mobility on the SiO_2 surface upon complexation by CO. *Chem. Commun.*, **46**, 976-978.
41. Hammer B., Norskov J. K. (1995) Why gold is the noblest of all the metals. *Nature*, **376**, 238-240.
42. Pellegrini R., Agostini G., Groppo E. et al (2011) 0.5% Pd/C catalyst for purification of terephthalic acid: irreversible deactivation in industrial plants. *J. Catal.*, **280**, 150-160.

43. Lazzarini A., Piovano A., Pellegrini R. et al (2016) A comprehensive approach to investigate the structural and surface properties of activated carbons and related Pd-based catalysts. *Catal. Sci. Technol.*, **6**, 4910-4922.
44. Bond G. C., Webb G., Wells P. B. et al (1962) Patterns of behavior in catalysis by metals. *J. Catal.*, **1**, 74-84.
45. McCue A. J., Anderson J. A. (2015) Recent advances in selective acetylene hydrogenation using palladium containing catalysts. *Front. Chem. Sci. Eng.*, **9**, 142-153.
46. Soldatov A., Della Longa S., Bianconi A. (1993) Relevant role of hydrogen atoms in the XANES of Pd hydride: Evidence of hydrogen induced unoccupied states. *Solid State Commun.*, **85**, 863-868.
47. Scarano D., Bordiga S., Lamberti C. et al (2006) Hydrogen adsorption and spill-over effects on H-Y and Pd-containing Y zeolites: An experimental and theoretical investigation. *Appl. Catal. A*, **307**, 3-12.
48. Tew M. W., Miller J. T., van Bokhoven J. A. (2009) Particle size effect of hydride formation and surface hydrogen adsorption of nanosized palladium catalysts: L_3 edge vs K edge X-ray absorption spectroscopy. *J. Phys. Chem. C*, **113**, 15140-15147.
49. Bugaev A. L., Guda A. A., Lomachenko K. A. et al (2014) Temperature- and pressure-dependent hydrogen concentration in supported PdHx nanoparticles by Pd K-edge X-ray absorption spectroscopy. *J. Phys. Chem. C*, **118**, 10416-10423.
50. Wang J. Q., Wang Q., Jiang X. H. et al (2015) Determination of nanoparticle size by measuring the metal-metal bond length: the case of palladium hydride. *J. Phys. Chem. C*, **119**, 854-861.
51. Bugaev A. L., Guda A. A., Lazzarini A. et al (2016) In situ formation of hydrides and carbides in palladium catalyst: When XANES is better than EXAFS and XRD. *Catal. Today*, 10.1016/j.cattod.2016.1002.1065.
52. Teschner D., Borsodi J., Wootsch A. et al (2008) The roles of subsurface carbon and hydrogen in palladium-catalyzed alkyne hydrogenation. *Science*, **320**, 86-89.
53. Tew M. W., Janousch M., Huthwelker T. et al (2011) The roles of carbide and hydride in oxide-supported palladium nanoparticles for alkyne hydrogenation. *J. Catal.*, **283**, 45-54.
54. Tew M. W., Nachtegaal M., Janousch M. et al (2012) The irreversible formation of palladium carbide during hydrogenation of 1-pentyne over silica-supported palladium nanoparticles: in situ Pd K and L_3 edge XAS. *Phys. Chem. Chem. Phys.*, **14**, 5761-5768.
55. Johnson A. D., Daley S. P., Utz A. L. et al (1992) The chemistry of bulk hydrogen - reaction of hydrogen embedded in nickel with adsorbed CH_3. *Science*, **257**, 223-225.
56. Yamauchi M., Ikeda R., Kitagawa H. et al (2008) Nanosize effects on hydrogen storage in palladium. *J. Phys. Chem. C*, **112**, 3294-3299.
57. Joly Y., Grenier S. (2016) Theory of X-Ray Absorption Near Edge Structure. In van Bokhoven J. A. and Lamberti C. (eds), X-Ray Absorption and X-Ray Emission Spectroscopy: Theory and Applications, John Wiley & Sons, Chichester (UK), pp. 73-97.
58. Guda S. A., Guda A. A., Soldatov M. A. et al (2015) Optimized finite difference method for the full-potential XANES simulations: application to molecular adsorption geometries in MOFs and metal-ligand intersystem crossing transients. *J. Chem. Theory Comput.*, **11**, 4512-4521.
59. Ramaker D. E., Koningsberger D. C. (2010) The atomic AXAFS and $\Delta\mu$ XANES techniques as applied to heterogeneous catalysis and electrocatalysis. *Physical Chemistry Chemical Physics*, **12**, 5514-5534.
60. Bus E., Ramaker D. E., van Bokhoven J. A. (2007) Structure of ethene adsorption sites on supported metal catalysts from in situ XANES analysis. *J. Am. Chem. Soc.*, **129**, 8094-8102.
61. Guo N., Fingland B. R., Williams W. D. et al (2010) Determination of CO, H_2O and H_2 coverage by XANES and EXAFS on Pt and Au during water gas shift reaction. *Phys. Chem. Chem. Phys.*, **12**, 5678-5693.
62. Szlachetko J., Sa J., Safonova O. V. et al (2013) In situ hard X-ray quick RIXS to probe dynamic changes in the electronic structure of functional materials. *J. Electron Spectrosc. Relat. Phenom.*, **188**, 161-165.
63. Glatzel P., Singh J., Kvashnina K. O. et al (2010) In Situ Characterization of the 5d Density of States of Pt Nanoparticles upon Adsorption of CO. *J. Am. Chem. Soc.*, **132**, 2555-2557.
64. Janssens T. V. W., Falsig H., Lundegaard L. F. et al (2015) A consistent reaction scheme for the selective catalytic reduction of nitrogen oxides with ammonia. *ACS Catal.*, **5**, 2832-2845.
65. Schlogl R. (2015) Heterogeneous catalysis. *Angew. Chem.-Int. Edit.*, **54**, 3465-3520.
66. Lamberti C., Prestipino C., Bonino F. et al (2002) The chemistry of the oxychlorination catalyst: an in situ, time-resolved XANES study. *Angew. Chem. Int. Edit.*, **41**, 2341-2344.
67. Groppo E., Uddin M. J., Bordiga S. et al (2008) Structure and redox activity of copper sites isolated in a nanoporous P4VP polymeric matrix. *Angew. Chem.-Int. Edit.*, **47**, 9269-9273.
68. Muddada N. B., Olsbye U., Caccialupi L. et al (2010) Influence of additives in defining the active phase of the ethylene oxychlorination catalyst. *Phys. Chem. Chem. Phys.*, **12**, 5605-5618.

69. Muddada N. B., Olsbye U., Leofanti G. et al (2010) Quantification of copper phases, their reducibility and dispersion in doped-$CuCl_2/Al_2O_3$ catalysts for ethylene oxychlorination. *Dalton Trans.*, **39**, 8437-8449.
70. Bus E., Miller J. T., Jeremy Kropf A. et al (2006) Analysis of in situ EXAFS data of supported metal catalysts using the third and fourth cumulant. *Phys. Chem. Chem. Phys.*, **8**, 3248-3258.
71. Shannon S. L., Goodwin J. G. (1995) Characterization of catalytic surfaces by isotopic-transient kinetics during steady-state reaction. *Chem. Rev.*, **95**, 677-695.
72. Urakawa A., Burgi T., Baiker A. (2008) Sensitivity enhancement and dynamic behavior analysis by modulation excitation spectroscopy: Principle and application in heterogeneous catalysis. *Chem. Eng. Sci.*, **63**, 4902-4909.
73. Lamberti C., Zecchina A., Groppo E. et al (2010) Probing the surfaces of heterogeneous catalysts by in situ IR spectroscopy. *Chem. Soc. Rev.*, **39**, 4951-5001.
74. Yamamoto T., Suzuki A., Nagai Y. et al (2007) Origin and dynamics of oxygen storage/release in a Pt/ordered CeO_2-ZrO_2 catalyst studied by time-resolved XAFS analysis. *Angew. Chem.-Int. Edit.*, **46**, 9253-9256.
75. Oyama S. T., Li W. (1999) Absolute determination of reaction mechanisms by in situ measurements of reaction intermediates. *Top. Catal.*, **8**, 75-80.
76. Kopelent R., van Bokhoven J. A., Szlachetko J. et al (2015) Catalytically active and spectator Ce^{3+} in ceria-supported metal catalysts. *Angew. Chem.-Int. Edit.*, **54**, 8728-8731.
77. Nachtegaal M., Müller O., König C. et al (2016) QEXAFS: Techniques and Scientific Applications for Time-Resolved XAS. In van Bokhoven J. A. and Lamberti C. (eds), X-Ray Absorption and X-Ray Emission Spectroscopy: Theory and Applications, John Wiley & Sons, Chichester (UK), pp. 155-183.
78. Mathon Olivier, Kantor I., Pascarelli S. (2016) Time-Resolved XAS Using an Energy Dispersive Spectrometer: Techniques and Applications. In van Bokhoven J. A. and Lamberti C. (eds), X-Ray Absorption and X-Ray Emission Spectroscopy: Theory and Applications, John Wiley & Sons, Chichester (UK), pp. 185-212.
79. Su X. C., Cremer P. S., Shen Y. R. et al (1997) High-pressure CO oxidation on Pt(111) monitored with infrared-visible sum frequency generation (SFG). *J. Am. Chem. Soc.*, **119**, 3994-4000.
80. Ta N., Liu J. Y., Chenna S. et al (2012) Stabilized gold nanoparticles on ceria nanorods by strong interfacial anchoring. *J. Am. Chem. Soc.*, **134**, 20585-20588.
81. Braglia L., Bugaev A. L., Lomachenko K. A. et al (2016) Investigation of oxygen vacancies in CeO_2/Pt system with synchrotron light techniques. *J. Phys: Conf. Series*, **712**, art. n. 012064.
82. Chen L. X. (2016) X-Ray Transient Absorption Spectroscopy. In van Bokhoven J. A. and Lamberti C. (eds), X-Ray Absorption and X-Ray Emission Spectroscopy: Theory and Applications, John Wiley & Sons, Chichester (UK), pp. 213-249.
83. Gawelda W., Szlachetko J., Milne C. J. (2016) X-Ray Spectroscopy at Free Electron Lasers. In van Bokhoven J. A. and Lamberti C. (eds), X-Ray Absorption and X-Ray Emission Spectroscopy: Theory and Applications, John Wiley & Sons, Chichester (UK), pp. 637-669.
84. Borfecchia E., Garino C., Salassa L. et al (2013) Synchrotron ultrafast techniques for photoactive transition metal complexes. *Phil. Trans. R. Soc. A*, **371**, art. n. 20120132.
85. Chergui M. (2014) Emerging photon technologies for chemical dynamics. *Faraday Discuss.*, **171**, 11-40.
86. Ferey G. (2008) Hybrid porous solids: past, present, future. *Chem. Soc. Rev.*, **37**, 191-214.
87. Long J. R., Yaghi O. M. (2009) The pervasive chemistry of metal-organic frameworks. *Chem. Soc. Rev.*, **38**, 1213-1214.
88. Butova V. V., Soldatov M. A., Guda A. A. et al (2016) Metal-Organic Frameworks: Structure, Properties, Synthesis, and Characterization. *Russ. Chem. Rev.*, **85**, 280-307.
89. Borfecchia E., Braglia L., Bonino F. et al (2016) Probing structure and reactivity of metal centers in metal-organic frameworks by XAS techniques. In Iwasawa Y., Asakura K., and Tada M. (eds), XAFS techniques for catalysts, nanomaterials, and surfaces, Springer, pp. doi: 10.1007/1978-1003-1319-43866-43865_43826.
90. Corma A., Garcia H., Xamena F. (2010) Engineering metal organic frameworks for heterogeneous catalysis. *Chem. Rev.*, **110**, 4606-4655.
91. Ranocchiari M., van Bokhoven J. A. (2011) Catalysis by metal-organic frameworks: fundamentals and opportunities. *Phys. Chem. Chem. Phys.*, **13**, 6388-6396.
92. Yoon M., Srirambalaji R., Kim K. (2012) Homochiral metal-organic frameworks for asymmetric heterogeneous catalysis. *Chem. Rev.*, **112**, 1196-1231.
93. Vermoortele F., Valvekens P., De Vos D. (2013) Catalysis at the metallic nodes of MOFs. In Llabrés i Xamena F. and Gascon J. (eds), Metal organic frameworks as heterogeneous catalysts, The Royal Society of Chemistry, pp. 268-288.
94. Falkowski J. M., Liu S., Lin W. (2013) Asymmetric catalysis with chiral metal organic frameworks. In Llabrés i Xamena F. and Gascon J. (eds), Metal organic frameworks as heterogeneous catalysts, The Royal Society of Chemistry, Cambridge, pp. 344-364.

95. Liu J. W., Chen L. F., Cui H. et al (2014) Applications of metal-organic frameworks in heterogeneous supramolecular catalysis. *Chem. Soc. Rev.*, **43**, 6011-6061.
96. Mondloch J. E., Farha O. K., Hupp J. T. (2013) Catalysis at the organic ligands. In Llabrés i Xamena F. and Gascon J. (eds), Metal organic frameworks as heterogeneous catalysts, The Royal Society of Chemistry, Cambridge, pp. 289-309.
97. Cavka J. H., Jakobsen S., Olsbye U. et al (2008) A new zirconium inorganic building brick forming metal organic frameworks with exceptional stability. *J. Am. Chem. Soc.*, **130**, 13850-13851.
98. Valenzano L., Civalleri B., Bordiga S. et al (2011) Disclosing the complex structure of UiO-66 MOF: a synergic combination of experiment and theory. *Chem. Mater.*, **23**, 1700-1718.
99. Chavan S., Vitillo J. G., Gianolio D. et al (2012) H_2 storage in isostructural UiO-67 and UiO-66 MOFs. *Phys. Chem. Chem. Phys.*, **14**, 1614-1626.
100. Jakobsen S., Gianolio D., Wragg D. S. et al (2012) Structural determination of a highly stable metal-organic framework with possible application to interim radioactive waste scavenging: Hf-UiO-66. *Phys. Rev. B*, **86**, Art. n. 125429.
101. Shearer G. C., Chavan S., Ethiraj J. et al (2014) Tuned to perfection: ironing out the defects in metal-organic framework UiO-66. *Chem. Mat.*, **26**, 4068-4071.
102. Øien S., Wragg D., Reinsch H. et al (2014) Detailed structure analysis of atomic positions and defects in zirconium metal-organic frameworks. *Cryst. Growth Des.*, **14**, 5370-5372.
103. Chavan S., Vitillo J. G., Uddin M. J. et al (2010) Functionalization of UiO-66 metal−organic framework and highly cross-linked polystyrene with $Cr(CO)_3$: In situ formation, stability, and photoreactivity. *Chem. Mater.*, **22**, 4602-4611.
104. Kandiah M., Nilsen M. H., Usseglio S. et al (2010) Synthesis and stability of tagged UiO-66 Zr-MOFs. *Chem. Mat.*, **22**, 6632-6640.
105. Kandiah M., Usseglio S., Svelle S. et al (2010) Post-synthetic modification of the metal-organic framework compound UiO-66. *J. Mater. Chem.*, **20**, 9848-9851.
106. Øien S., Agostini G., Svelle S. et al (2015) Probing reactive platinum sites in UiO-67 zirconium metal–organic frameworks. *Chem. Mater.*, **27**, 1042-1056.
107. Borfecchia E., Øien D., Svelle S. et al (2016) A XAS study of the local environment and reactivity of Pt-sites in functionalized UiO-67 MOFs. *J. Phys: Conf. Series*, **712**, art. n. 012125.
108. Braglia L., Borfecchia E., Lomachenko K. A. et al (2016) XAS on Rh and Ir metal sites in post synthetically functionalized UiO-67 Zirconium MOFs. *J. Phys: Conf. Series*, **712**, art. n. 012053.
109. Braglia L., Borfecchia E., Maddalena L. et al (2016) Exploring structure and reactivity of Cu-sites in functionalized UiO-67 MOFs. *Catal. Today*, doi 10.1016/j.cattod.2016.1002.1039.
110. Guda A. A., Guda S. A., Soldatov M. A. et al (2016) Finite difference method accelerated with sparse solvers for structural analysis of the metalorganic complexes. *J. Phys: Conf. Series*, **712**, Art. n. 012004.
111. Ramaker D. E. (2016) Novel XAS techniques for probing fuel cells and batteries. In van Bokhoven J. A. and Lamberti C. (eds), X-ray absorption and X-ray emission spectroscopy: theory and applications, John Wiley & Sons, Chichester (UK), pp. 485-522.